Nanoscale

PAPER

View Article Online
View Journal | View Issue

Cite this: *Nanoscale*, 2025, **17**, 9996

Co-doped perovskite nanocrystals for multiplexed anticounterfeiting applications†

Manoj Sharma, *[a] Chang Cao,[a] Gaveshana A. Sepalage,[a] Shi Tang,[b] Lan Nguyen,[a] Hao Deng,[a,c] Naufan Nurrosyid,[a] Junlin Yan,[a] Josh Moon,[a] Tuncay Alan,[c] James Andell Hutchison,[b] Paul Mulvaney[b] and Jacek J. Jasieniak *[a]

Received 17th December 2024,
Accepted 1st March 2025

DOI: 10.1039/d4nr05313c

rsc.li/nanoscale

Transition and lanthanide metal ion doping in colloidal perovskite nanocrystals results in efficient visible to near-infrared emission. Here, we explore the role of visible and near-infrared multi-emission pathways provided through Mn-doped and Yb–Mn co-doped perovskite nanocrystals within advanced photoluminescence-based security features. The features provide overt functionality through visible photoluminescence from the underlying Mn-dopants. Meanwhile, the Yb-dopants enable covert information to be concealed through their inherent near-infrared emission. These engineered printed patterns are assessed in terms of ambient, moisture, and thermal stability. Finally, the complexity of encryption is further enhanced by chemically engineering the host–dopant energy transfer processes through anion exchange reactions. This enables write and erase functions to be realised in these perovskite NC-based security features.

Introduction

The unauthorized replication of branded goods, medicines, certificates, banknotes, and other critical documents poses a severe global challenge, leading to billions of dollars in losses for governments and individuals.[1,2] Historically, these have been tagged using security features exhibiting fluorescence, optical interference, holographic, and other transduction mechanisms.[3] However, as the sophistication of forgers grows over time, there is a need to progressively increase the complexity of security features by introducing multilevel encryption features. This requires the development of advanced multiplexed approaches that combine overt and covert methods to enhance security, protection, and anti-counterfeiting measures.

Colloidal semiconductor nanocrystals (NCs) are nanoscale materials that have tunable optical and magnetic properties.[4–6] Among the wide library of colloidal nanocrystals, the perovskite class possesses exceptional optical and photoelectric properties due to their defect-tolerant nature.[7] The unique combination of spectrally tuneable and efficient fluorescence with a soft ionic lattice has created an opportunity to use these as fluorescent tags for multiplexed encryption.[2] Multiplexed security components within perovskite NCs can be achieved by precisely engineering their compositions to tune the emitted color and their decay lifetime. While typical perovskite NCs possess a single emission channel, the inclusion of dopant ions can introduce additional emission channels within the same perovskite NCs.[8–10] Doped perovskite NCs uniquely combine the high absorption ability of the perovskite host with the efficient emission from rare-earth and other metal ion dopants. The availability of suitable coordination numbers for rare-earth doping in perovskites offers a long-sought opportunity to harness the best properties of both the host and lanthanide dopant ions.[11] This feat has to date been unattainable with inorganic phosphors and traditional quantum dots.[12,13]

Foundational studies demonstrating perovskite-based security features have utilized core–shell $CsPbBr_3$@Cs_4PbBr_6/SiO_2 NCs, which exhibit the ability to switch their excitonic green emission under different conditions, including ultraviolet (UV) or near-infrared (NIR) excitation and variations in temperature.[14] Tailoring the monovalent A = FA or Cs cation in $APbBr_3$ NCs has been further shown to induce green emission, albeit with different luminescence decay lifetimes, thus

[a]*Department of Materials Science and Engineering, Monash University, Clayton, Victoria 3800, Australia. E-mail: manojsharma@monash.edu, Jacek.Jasieniak@monash.edu*
[b]*School of Chemistry and ARC Centre of Excellence in Exciton Science, University of Melbourne, Parkville, VIC, 3010, Australia*
[c]*Department of Mechanical and Aerospace Engineering, Monash University, Clayton, Victoria 3800, Australia*

†Electronic supplementary information (ESI) available: Supporting figures of TEM, XRD, XPS, UV visible absorbance and emission spectra, a table for lifetime decay components, additional images for security features, and stability tests. See DOI: https://doi.org/10.1039/d4nr05313c

enabling monocolor anticounterfeiting applications.[2] To increase the spectral range, a combination of $CH_3NH_3PbBr_3$-based perovskite NCs encapsulated in europium-based metal–organic frameworks (MOFs) was shown to induce multiple visible colors upon low and high-energy UV excitation.[15] To exploit both spectral and temporal ranges as vectors for anticounterfeiting in the visible region, bilayer combinations of green-emitting undoped $CsPbBr_3$ NCs with nanosecond lifetimes and orange-emitting Mn-doped $CsPbCl_3$ NCs with long millisecond lifetimes have been further used.[16]

In the literature for security applications, Yb dopant ions in different host semiconductors are mostly used to up-convert the NIR light into visible emission.[17–20] In recent years, successful sensitization of Yb dopants has been achieved in host $CsPbX_3$ (X = Cl, Br) perovskites through a defect-mediated down-conversion process, resulting in a photoluminescence quantum yield (PL QY) exceeding 100%.[8,11,21] This process relies on a single absorbed UV-blue photon being down-converted into two NIR photons *via* a pair of Yb ions through a quantum-cutting process.[8] Recently, the successful addition of multiple dopant ions (*e.g.* transition metal ion Mn and rare-earth metal ion Yb) into the $CsPbCl_3$ NC host was shown to provide down-converted triple emission (blue, orange, and NIR) under single wavelength excitation.[22] The lifetimes of these emission channels range from nanoseconds (blue) to milliseconds (orange and NIR), thus providing broad spectral and temporal tunability. Notably, co-doping that yields multi-emission pathways has also been demonstrated in double perovskite NCs and microcrystals, with examples including Bi^{3+} and Er^{3+}/Yb^{3+} doped $Cs_2AgInCl_6$, Cr^{3+} and Bi^{3+} doped $Cs_2Ag_{0.6}Na_{0.4}InCl_6$, and Eu^{3+} and Tb^{3+} doped $Cs_2NaInCl_6$:Sb^{3+} NCs.[23–25]

Here, we explore the use of multi-emission co-doped $CsPbX_3$ (X = Cl, Br) NCs as multimodal security features. As a baseline, Mn-doped and Mn–Yb co-doped $CsPbCl_3$ are synthesized by using a hot injection method. Through detailed morphological and photophysical studies, these materials are optimised to emit in the visible and NIR regions with high PL QYs under ultraviolet excitation. To develop security features, the doped colloidal NCs are further incorporated within fluorescent inks comprised of ethylene-vinyl acetate (EVA) as a binder. This results in highly efficient NCs with stable optical properties under ambient conditions. A further increase in the encryption capability is achieved by inducing a chemical activation and deactivation feature for the NIR emission. This work successfully utilizes both host and dopant functionalities to covertly encode anticounterfeiting measures within printed patterns.

Results and discussion

Mn- and Yb-doping into perovskite NCs rely on a lead substitution mechanism that can be induced by simply modifying the dopant/lead ratios during synthesis.[26] Here, both Mn-doped $CsPbCl_3$ and Mn–Yb-co-doped $CsPbCl_3$ NCs were synthesised by following a slightly modified hot-injection literature protocol that adopted this approach (see the Experimental section).[8] Fig. 1A shows a representative transmission electron microscopy (TEM) image of Mn–Yb-co-doped NCs. It is evident that these are ~9 nm and possess a cubic morphology. These characteristics are comparable to their doped and undoped counterparts, which are shown in Fig. S1.† Furthermore, powder X-ray diffraction (XRD) analysis confirms that the introduction of Mn and Yb does not modify the native cubic perovskite crystal structure (space group: *Pm*3*m*) of the undoped $CsPbCl_3$ NCs.[22,27] However, in the doped and co-doped $CsPbCl_3$ NCs, a reduced lattice parameter is observed compared to the undoped sample, as evidenced by the diffraction peaks shifting to higher scattering angles. Elemental characterization using inductively coupled plasma mass spectroscopy (ICP-MS) and X-ray photoelectron spectroscopy (XPS) was conducted for both doped and co-doped samples. ICP-MS analysis reveals the doping levels relative to the total B-site cations in the NCs (*e.g.* Mn (%) = Mn/(Mn + Pb) and Yb (%) = Yb/(Yb + Mn + Pb)). For Mn in the doped NCs it was 5.9%, while for Mn and Yb in the co-doped NCs it was 4.8% and 6.9%, respectively. The high-resolution XPS spectra for the Mn 2p and Yb 4d orbitals, shown in Fig. S3,† further confirm the successful doping of these metal ions into the perovskite NCs; however, at the studied doping levels, determination of their oxidation states was not possible.[22,27,28]

Fig. 1B and C show the absorbance and photoluminescence (PL) emission spectra for the Mn-doped and Mn–Yb co-doped samples, respectively. The absorbance spectra show a sharp excitonic peak at ~398 nm for both samples, which is slightly blue-shifted as compared to undoped $CsPbCl_3$ NCs (Fig. S4†). This is consistent with doping-induced lattice contraction leading to a slight change in the bandgap of doped NCs.[29,30] The PL emission spectra of doped NCs exhibit dual emission at ~405 nm and ~600 nm. Meanwhile, the codoped NCs show triple emission at ~405 nm, ~600 nm, and ~990 nm, corresponding to the recombination of photoexcited electrons through the band edge, Mn dopants, and Yb dopants, respectively. The absolute PL QYs are measured with an integrating sphere in the visible region. The calculated values are 20.6% for the doped samples, and 11.5% for the co-doped samples, respectively. The NIR PL QY for Yb–Mn co-doped NCs in the NIR region is approximately 118%, estimated relative to the visible PL QY using a calibrated silicon detector (Fig. S5 and 6†). As a reference for Yb dopant emission, the PL QY of only Yb-doped $CsPbCl_3$ NCs in the NIR region was calculated to be ~148% (Fig. S6†). The above unity PL QY for NIR emission is direct evidence for quantum-cutting in these materials, despite the co-doped nature. Representative digital micrographs of both samples under high-energy excitation using a visible and infrared (IR) camera are shown in Fig. 1D. This comparison clearly shows the bright orange emission from Mn-dopant ions and the selective Yb NIR emission in the co-doped samples.

The photoexcitation of doped perovskite NCs and energy transfer processes from host perovskite NCs to Mn and Yb

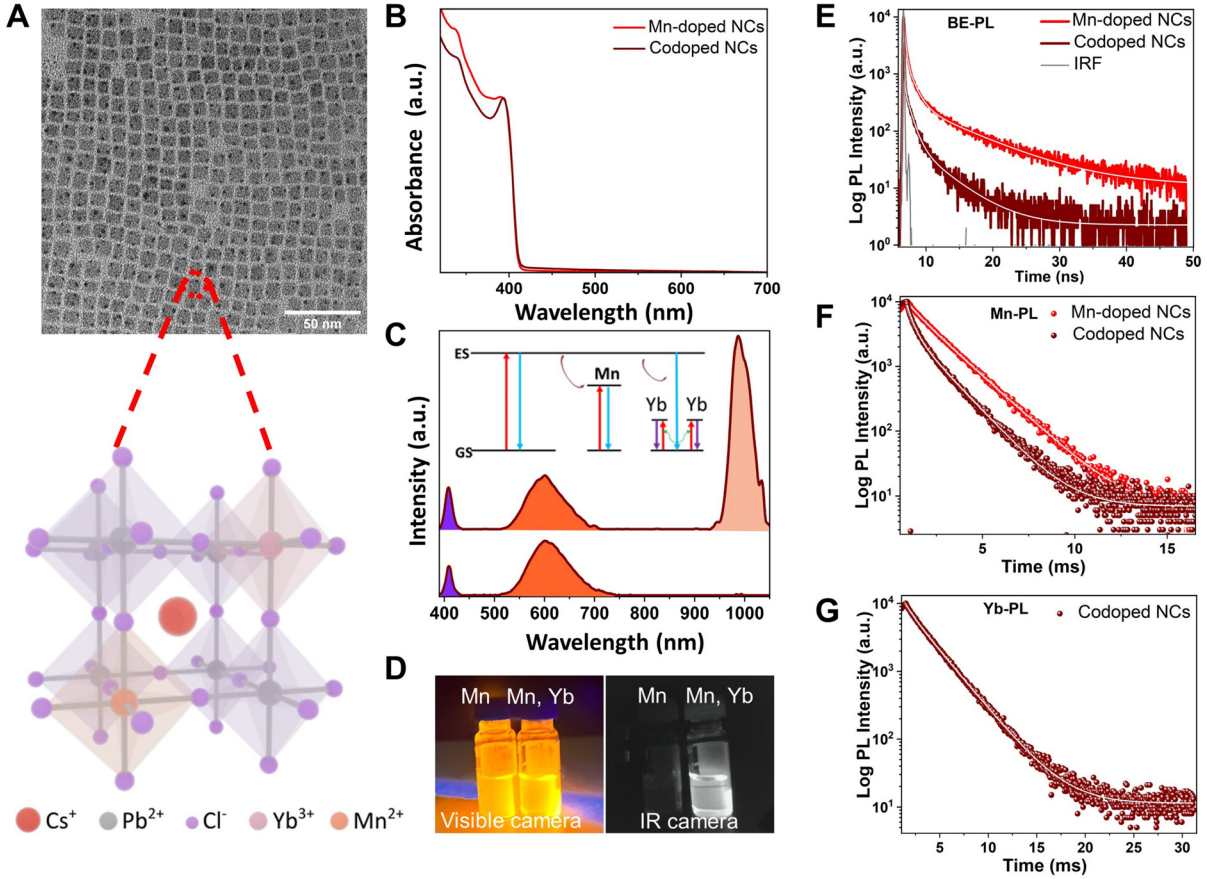

Fig. 1 (A) TEM image and schematic of the co-doped perovskite structure. (B and C) UV-visible absorption spectra and PL emission spectra of Mn-doped and Yb, Mn co-doped $CsPbCl_3$ NCs (the inset in C shows the energy transfer pathways for multi-emission NCs). (D) digital images of doped and co-doped NCs recorded using visible and IR cameras, with the latter utilizing a visible long pass filter. Time-resolved decay curves of Mn-doped and Yb, Mn co-doped $CsPbCl_3$ NCs using the (E) band edge, (F) Mn-dopant, and (G) Yb-emissions.

dopants have been widely discussed in the literature.[8,22,27,31–33] These have indicated that while the energy transfer from the host to Mn follows a Dexter-type energy transfer process, Yb-PL is sensitized through a mediating shallow trap state below the conduction band. Fig. 1E–G show the excitonic, Mn-dopant, and Yb-dopant-related time-resolved photoluminescence (TRPL) decay curves of the doped and/or co-doped NCs, respectively. The average exciton emission lifetime is ~3.0 ns and ~0.7 ns for doped and co-doped NCs. The acceleration of excitonic recombination in co-doped NCs suggests faster depletion of excitons to multiple dopant states as compared to singly-doped NCs.[8,22] Meanwhile, the average lifetime of Mn-dopant PL is six orders of magnitude longer, with the co-doped NCs exhibiting a slightly accelerated lifetime of 1.2 ms *versus* 1.6 ms for the singly doped NCs. This slight variation might arise due to the variability of Mn doping amounts in these samples or inter-dopant energy transfer.[22] Finally, the Yb-dopant PL in the NIR for co-doped samples shows a long millisecond lifetime of 2.0 ms. The details of the average lifetime and their components are shown in the ESI (Tables S1 and 2†). While the mechanistic aspects to elucidate the exact origins of these lifetime differences are outside the scope of this work, the results clearly indicate that the large spectral and temporal windows provide significant scope for use in multi-dimensional security.

The process for writing covert and overt written information on a glass substrate using doped perovskite NC inks is shown in Fig. 2A. Firstly, the synthesised doped and co-doped NCs are introduced into inks suitable for prototype security features using an EVA-based commercial hot melt binder (see the Experimental section). The inks themselves retain the characteristic NC optical properties, as seen from the visible emission under UV excitation shown in Fig. 2B, as well as absorption and emission spectra presented in Fig. S7.† The inks are subsequently coated on a substrate that possesses a selective mask to impart patterning and cured at 70 °C. Depending on the type of ink used, covert and overt features can be realised. Fig. 2 shows the digital images of written characters with a combination of doped and co-doped NC inks. In this example, two words MONASH and EXCITON have been chosen, with the O and N characters patterned using a co-doped NC ink, while all other characters contain only the Mn-doped NC ink. The images are obtained by illuminating the patterned substrates with a UV torch and imaged using a typical mobile phone

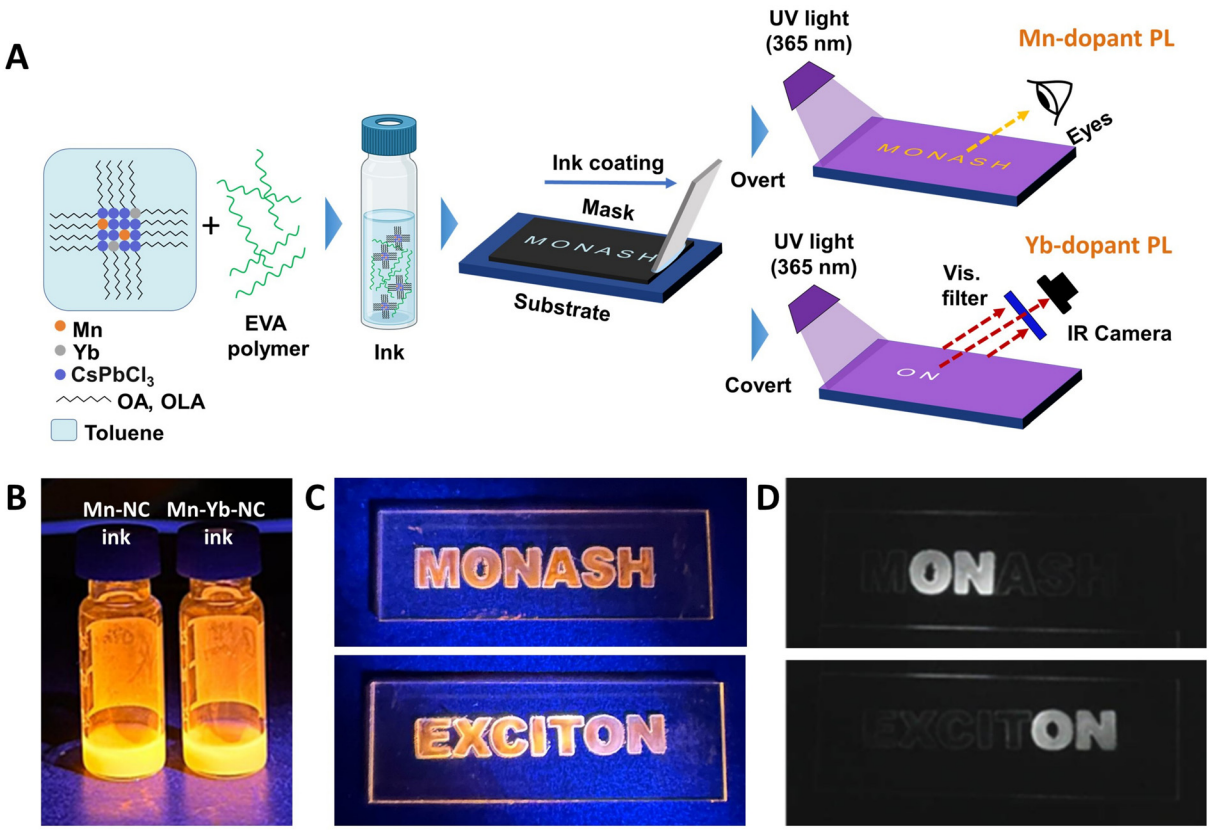

Fig. 2 (A) Schematic for the fabrication of perovskite NC security features with overt and covert functionalities. (B) Digital images of Mn-doped and Mn–Yb codoped NC inks under UV excitation. Digital images of written characters excited under UV light taken with (C) a visible camera and (D) an IR camera coupled with a visible cut-off filter.

camera (Fig. 2C) and a hand-held IR camera with a visible long pass filter (Fig. 2D and video S1 in ESI†). Co-doped NCs possessing both visible and NIR emissions can conceal the covert information. In our IR optical detection setup, the visible signal is filtered out, ensuring that only the NIR emissive features are captured. At the same time, the visible orange emission for the characters O and N blends seamlessly with the other characters that have been created using inks of singly doped NCs.

To characterize the photoluminescence properties of the individual characters, the NC inks were drop cast onto pre-patterned polyacrylic slides and imaged with a hyperspectral camera coupled with a microscope. The imaging layout is shown in Fig. 3A, with the excitation source being a 365 nm LED. Fig. 3B and C show the recorded normalised PL emission spectra for individual characters with visible and short-wave infrared (SWIR) detectors. All characters show similar orange emissions corresponding to Mn dopant transitions. Meanwhile, the characters O and N possess additional NIR emission due to Yb co-doping. The corresponding digital images of these characters with both visible and SWIR cameras are shown in Fig. 3D and E. The images validate the hyperspectral imaging, clearly showing the Mn emission for all characters and the selective Yb emission for O and N. Notably, some inhomogeneity is observed in the characters at this resolution; however, the high signal to background levels dictate that this is not a practical issue for achieving optical read-out.

The utility of these doped and co-doped NC security features for various security applications is predicated on their stability. In general, perovskite NCs possess poor environmental stability because of their soft ionic lattice.[34–36] However, the engineered doped and co-doped NC composites are observed to exhibit markedly improved stability under ambient and humid conditions. This is demonstrated in Fig. S8,† which shows that the written patterns are stable under ambient conditions with minimal degradation to their visible and NIR emission after over six months. Furthermore, the patterns were dipped in water for a period of 10 days and imaged with visible and IR cameras. The samples showed good stability over extended periods of direct immersion (see Fig. 4A), but eventually exhibited degradation by day 10 (see Fig. S9†). We conducted more detailed short-term stability tests by depositing the NCs and NC-EVA composite onto glass slides and exposing them to water, as well as another common solvent, ethanol. The PL emission spectra and digital images with visible and IR cameras were recorded at different time intervals (see Fig. S10 and 11†), with summaries included in

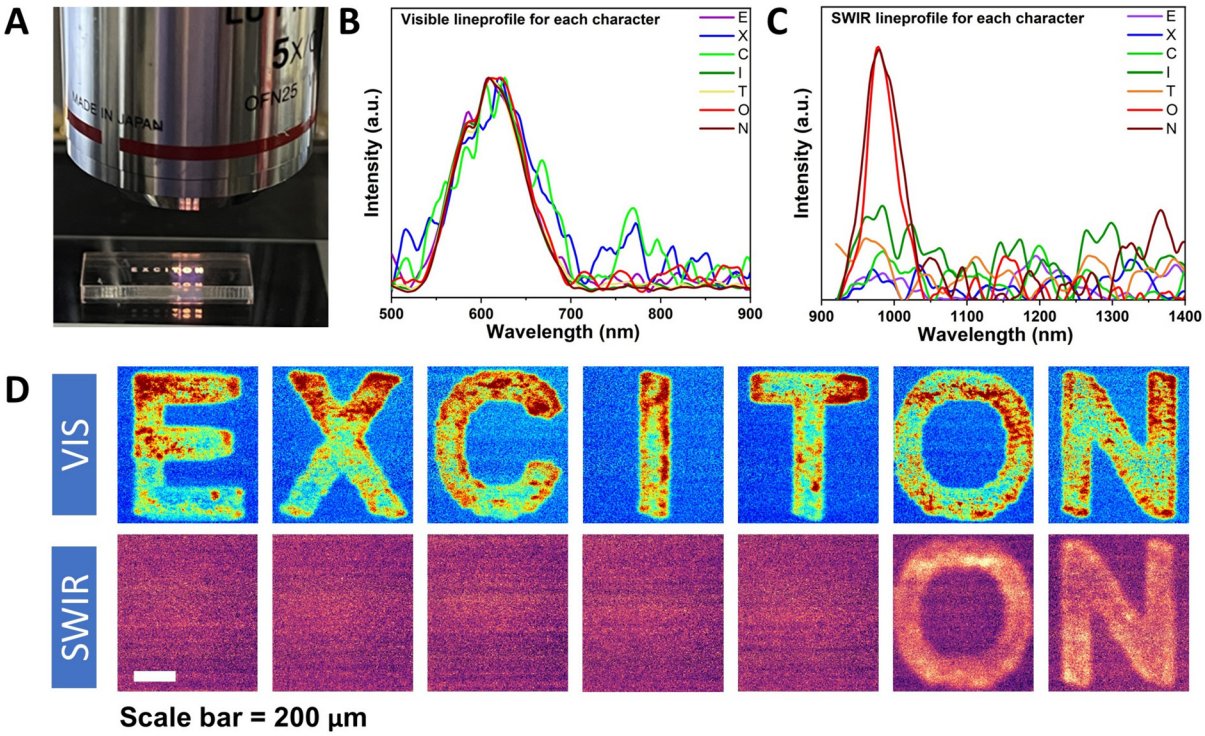

Fig. 3 PL emission spectra and imaging using a hyperspectral camera. (A) Digital image of written letters under UV-excitation. (B and C) PL emission spectra integrated over the area of each individual letter using visible and SWIR detectors. Digital images of individual characters under (D) visible and (E) SWIR detectors.

Fig. 4B. These measurements confirm that both Mn and Yb dopant emission intensities and spectral profiles remained stable for NC-EVA during the testing periods in both polar solvents. In contrast, both visible and IR emissions are quenched in less than ~1 minute for bare NCs. This indicates that the developed security features matched well to practical terrestrial environments, even when operating under high humidity or underwater.

Finally, the NC inks were tested for their stability up to a modest operating temperature of 150 °C as shown in Fig. 4C. The PL emission spectra during a typical thermal cycle is shown for both Mn and Yb dopant emission peaks in Fig. S12.† It indicates negligible spectral shifting of either peak with increasing or decreasing temperature. This thermal cycle is imaged in Fig. 4C, showing that when excited with a UV LED, both Mn and Yb dopant emissions are retained. To quantify the change in the PL emission intensity with temperature, the NIR emission intensity was recorded with an IR camera and is presented in Fig. 4D. It shows that the NIR PL is enhanced by ~61% when the temperature is increased up to 150 °C and then drops back to its original values during the down cycle. Previous studies have reported an increase in Yb dopant-related PL with a moderate rise in temperature of up to 100 °C.[37] This enhancement has been attributed to the partial removal of surface-adsorbed water, which is known to quench Yb-PL. In Fig. S11,† Mn-PL has been quantified relative to the total integrated PL intensity. Unlike Yb-PL, Mn-PL shows a slight decrease at higher temperatures. This is consistent with previous reports.[37,38] Overall, our temperature-dependent results indicate that the EVA-based copolymers preserve the integrity of the NCs, even at elevated temperatures. This finding highlights their suitability for modest-temperature printing processes, thereby expanding the potential applications of these NC composites to a broad range of security applications.

The ability to read, write, and erase information is a key requirement for advanced security features.[3,14] To further increase the level of encryption, here we demonstrate that write and erase functions can be integrated into these features through a chemical treatment that induces anion exchange of the NCs within the written patterns (Fig. 5). It has been widely reported that perovskite NCs can undergo a room-temperature anion exchange process when exposed to alternative anions compared to those in their lattice.[39,40] The sensitivity of the perovskite bandgap to the halide enables a tunable bandgap across the entire visible spectrum. To demonstrate this, doped and co-doped NCs are selectively patterned in a square array to show typical Mn-induced orange and Yb-induced NIR emission when excited with UV light. Fig. 5A shows the exposure of the patterns to a Br-based anion precursor for less than 10 seconds. It evidently induces a change in the emission colour from orange to green for all the patterned squares filled with NC composites. Importantly, this exchange process induces the concurrent disappearance of the orange emission and NIR

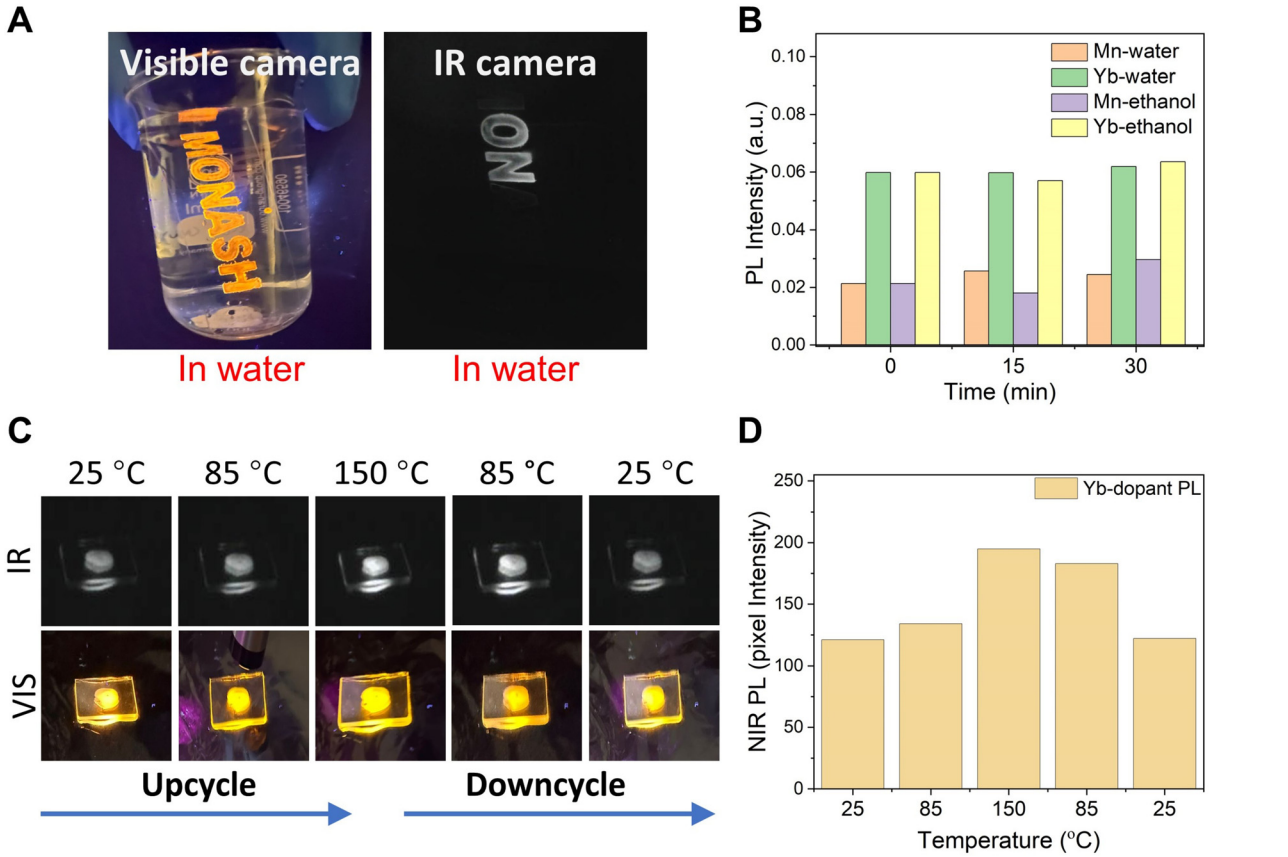

Fig. 4 Stability studies of encrypted writing using NC composites. (A) Digital images using a visible and IR camera for encrypted patterns dipped in water. (B) Variation in the PL intensity as a function of immersion time. (C) Digital images of NC composites captured using visible and IR cameras at different temperatures. (D) Relative NIR PL intensity measured at different temperatures during heating (upcycle) and cooling (downcycle) cycles as compared to its starting value.

emission from Mn- and Yb-dopant ions. This observation is consistent with recent studies, which have proposed that a decrease in the bandgap due to anion exchange from Cl to Br results in back energy/charge transfer from dopant ions or defect states, leading to a significant reduction in PL emission for individual Mn and Yb dopants.[10,31,41,42] Reversing the ion exchange process through exposure to a Cl-based anion solution can partially re-activate this Yb emission revealing the NIR encrypted information (Fig. S13†). Fig. 5B and C shows the PL emission spectra of these doped and co-doped NC composites undergoing anion exchange with Br- and Cl-precursors. Consistent with the observations from the visible and IR images, the PL emission spectra also show the disappearance of Mn and Yb dopant emissions with Br treatment and partial recovery of these with reverse Cl treatment. We envision that further engineering in designing perovskite NC inks that enable reversible anion exchange will lead to the full utilization of these emerging doped perovskite NCs for security applications.

In summary, we have shown that Mn^{2+} doped and Mn^{2+} and Yb^{3+} co-doped inorganic $CsPb(Br,Cl)_3$ perovskite NCs can be utilised in advanced photoluminescence-based security features. When incorporated in simple ethylene-vinyl acetate-based composites, these NCs show suitable ambient, moisture, and temperature stability for practical implementation within terrestrial environments. The security features harness the orange emission stemming from the Mn^{2+} dopants, which is further augmented to provide an additional NIR emission channel through the inclusion of Yb^{3+} within the co-doped NCs. This multi-emission tunability has been exploited to demonstrate the encoding of covert information in the NIR. We have further demonstrated that these perovskite host emissions can be externally controlled by altering the chemical environment with a facile halide exchange reaction. This externally controlled activation/deactivation of the dopant emission enables the seamless integration of read-out and erase functions. Overall, the unique appearance of multi-emission spanning across visible to NIR regions of the spectrum from a doped perovskite nanocrystal system has the potential to covertly encode information within printed security features. Further efforts in the engineering of perovskite-based host-dopant ion combinations could enable multilevel encryption based on light emission color, lifetime, and chemical activation. Overall, this work uniquely positions these emerging doped perovskite NCs as next-generation security tags.

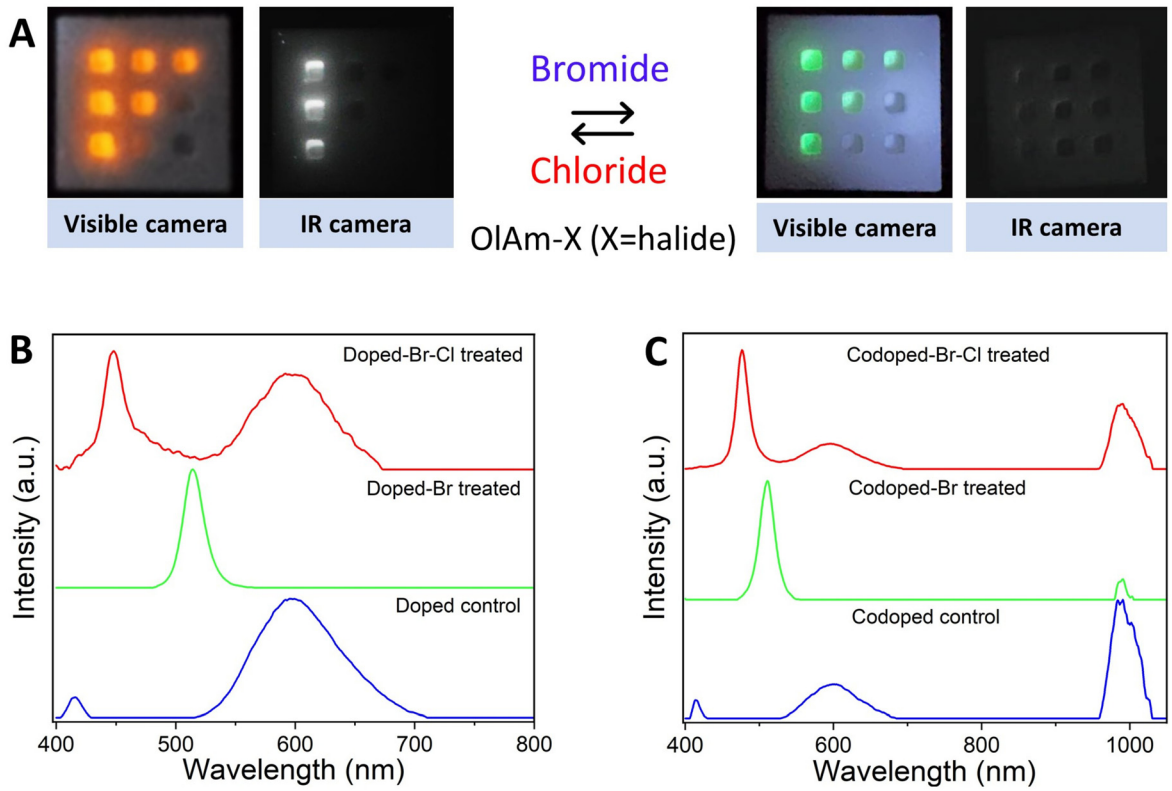

Fig. 5 Halide exchange reactions to erase and partially re-activate the secret encrypted information. (A) Visible and IR camera images of square boxes filled with doped and codoped NCs during continuous anion exchange with bromide and chloride precursors. (B and C) PL emission spectra of doped and codoped NCs during continuous anion exchange with Br and Cl precursors.

Experimental section

Chemicals

Lead acetate trihydrate ($Pb(OAc)_2{\cdot}3H_2O$) (99.9%), ytterbium acetate hydrate [$Yb(OAc)_3{\cdot}xH_2O$] (99.9%), manganese(II) acetate tetrahydrate ($Mn(OAc)_2{\cdot}4H_2O$, 99.999%), cesium acetate (CsOAc) (99.9%), trimethylsilyl chloride (TMS-Cl) (98%), oleic acid (OA) (90%), oleylamine (OAm, 70–80%), octadecene (ODE, 90%), analytical grade hexanes, ethanol, and ethyl acetate (EtOAc) (99%) were all obtained from Sigma Aldrich.

Synthesis of doped NCs

Control undoped, Mn-doped, and Mn–Yb co-doped $CsPbCl_3$ NCs were synthesized by following the hot injection method outlined in the literature with few modifications.[8] Briefly, 0.2 mmol $Pb(OAc)_2{\cdot}3H_2O$ (75.9 mg), 0.16 mmol $Yb(OAc)_3{\cdot}xH_2O$ (67.5 mg), 0.016 mmol $Mn(OAc)_2{\cdot}4H_2O$ (4 mg) and 0.28 mL of 1 M CsOAc dissolved in ethanol (53.7 mg) were added to a 50 mL round bottom flask containing 5 mL of ODE, 1 mL of OA, and 0.5 mL of OAm. The reaction vessel was evacuated and degassed at 120 °C for 1 hour. Subsequently, the flask was switched to nitrogen and heated to 240 °C, at which point 0.2 mL of TMS-Cl in 0.5 mL ODE was swiftly injected. This is followed by quenching the reaction with an ice bath. For Mn-doped NCs, the Yb precursor is not added at the start. Undoped $CsPbCl_3$ NCs were also synthesized using the same protocol, excluding $Yb(OAc)_3{\cdot}xH_2O$ and $Mn(OAc)_2{\cdot}4H_2O$, and using only 0.24 mL of 1 M CsOAc in ethanol.

To purify the assynthesised NCs, the crude reaction solution was centrifuged for 10 min at 7000 rpm. This was followed by discarding the supernatant and the settled white precipitate was dissolved in 10 mL hexane. Secondly, the solutions were centrifuged again for 10 min at 4500 rpm and the clear supernatant solution was kept and filtered through a 0.25 μm filter. This is necessary to filter out larger-sized subpopulations. For removing the excess ligands and unreacted/surface adsorbed salts, the final NCs were precipitated with EtOAc and finally dispersed in hexane/toluene for further characterization and measurements. For ambient storage, the doped NC solution was dried and resuspended in an anhydrous solvent.

EVA-based doped NC inks

The synthesized doped and co-doped NCs were dissolved in toluene (20 mg ml^{-1}). The binder solution was prepared by dissolving a commercial hot melt material (HM 6542) in toluene (400 mg ml^{-1}). The hotmelt was purchased from Nanpao, Taiwan, and used as received. It contains EVA (40%) and hydrogenated petroleum resin (60%). The solution was prepared by stirring at 90 °C until it made a clear solution. Then the doped and co-doped NC solution and the binder solution

were mixed in a desired ratio of 1 : 1 and stirred at room temperature to make an ink solution. For the printing of the letters, a mask was prepared by pasting two layers of electrical insulation tapes on glass, and the letters were laser cut. Once the cut sections were removed, those openings were filled with the ink solution using a selective mask for different letters. Then the printed plate was placed on a hot plate at 70 °C for 10 min under N_2 flow. Once dried, the mask was carefully removed.

Anion exchange reactions

Oleylammonium halide (OLAM-X) (X = Cl, Br) was used as a precursor for anion exchange reactions and was synthesised by following a literature method.[43] Anion exchange reactions were conducted on encrypted patterns filled selectively with Mn-doped $CsPbCl_3$ and Mn–Yb-co-doped $CsPbCl_3$ NC samples. Briefly, 25 mg of oleylammonium bromide (OLAM-X) in 1 mL toluene was mixed by stirring and ultrasonicating for 15 min under ambient conditions. Variable amounts (*e.g.* 5 μL–20 μL) of OLAM-X precursor were added dropwise on doped NC-based patterns and its optical properties were continuously measured.

Characterization

Powder X-ray diffraction (XRD) samples were prepared by drop-casting a dispersion of perovskite nanocrystals onto a glass substrate, followed by drying under ambient conditions without heating. XRD patterns were recorded using a Bruker D8 Advance diffractometer equipped with a Cu-Kα radiation source (40 kV, 40 mA) and a high-speed position-sensitive Lynxeye XE line detector. A Tecnai G2 T20 TWIN (FEI Company) microscope equipped with a LaB_6 electron emitter was used to record the TEM images of the studied samples. All X-ray photoelectron spectroscopy (XPS) spectra of the doped and co-doped samples were recorded using a Thermo Nexsa surface analysis system equipped with an Al Kα X-ray source. The measurement was conducted with a chamber pressure $<5.0 \times 10^{-8}$ Torr. ICP-MS measurements were conducted using an Agilent 8900 triple quadrupole ICP-MS system. For sample preparation, each sample was vigorously shaken before pipetting 0.4 mL into a hot block tube. Into each tube 2 ml of Milli-Q water was added and mixed with the sample. The tubes were placed in a hot block digester and heated at 80 °C to evaporate the hexane. The solutions were then made up to 20 ml volume in 2% HNO_3. ICP-MS analysis of the desired elements (*e.g.* Cs, Pb, Mn, Yb) was done on a diluted (×10) and undiluted basis.

UV-Visible absorbance spectra of all studied samples were collected using a PerkinElmer Lambda 950 UV-Vis-NIR spectrometer in the solution form. The steady-state emission spectra in the visible-NIR region were recorded with a commercial spectrometer (Stellar Net) equipped with a CCD camera (Silver-Nova-TEC-X2), using a 380 nm excitation source (SL1-LED), respectively. The detector has been calibrated using a calibrated light source (*e.g.* SL1-CAL) in the range of 300–1100 nm. PL spectra and PL QYs in the visible region were also obtained using a Horiba Fluoromax-4 spectrofluorometer. TRPL was measured with a FluoTime 300 time-correlated single photon counting (TCSPC) system using 370 nm UV laser excitation (Pico Quant Co., Ltd, Berlin, Germany).

Setup for detecting IR images

Detection of IR images from written patterns and characters was achieved by following a recent study by Dogan *et al.*[44] Briefly, a 60-fps NIR camera (ArduCam with OV23113) coupled with a long pass visible filter and a 10 W 365 nm UV LED was used to record the NIR images by filtering the visible emission.

Hyperspectral imaging

The QD solutions were drop cast onto the pre-patterned polyacrylic slides and the process was repeated three times to allow sufficient infill into each character. The image was acquired with PhysSpec software through a Photon Etc. IMA hyperspectral imager, coupled to a Nikon ECLIPSE LV100ND microscope. iXon Ultra 888 EMCCD and ZephIR 1.7 cameras were used for visible and SWIR imaging, respectively. A 365 nm LED (Thorlabs, M365L3) was used as an excitation source which was coupled to the microscope through a collimation adapter (Thorlabs, COP5-A).

Author contributions

M. Sharma initiated the project and designed the experiments with J. J. Jasieniak. M. Sharma and C. Cao performed the synthesis. M. Sharma performed steady-state and TRPL measurements. C. Cao performed TEM measurements. G. A. Sepalage printed security features and assisted in ink preparations and anti-counterfeiting studies. S. Tang performed the hyperspectral imaging for security patterns with inputs from J. A. Hutchison. L. Nguyen, and H. Deng under the supervision of T. Alan assisted in IR imaging and related characterizations. N. Nurrosyid performed the XRD measurements. J. Yan performed the XPS measurements. J. Moon synthesized the anion exchange precursors. P. Mulvaney assisted with PL QY measurements and analysis of photophysical results. M. Sharma and J. J. Jasieniak analysed and worked on the manuscript with assistance from all other authors. J. J. Jasieniak supervised the whole project.

Data availability

All the data related to the present work are included in the manuscript. The data supporting this article have been included as part of the ESI† and plotted with the help of Origin software and Avantage. Analysis and quantification of images were performed using ImageJ software. The data will be made available upon request to the corresponding author.

Conflicts of interest

There are no conflicts to declare.

Acknowledgements

This work was funded by the Australian Research Council (ARC) Centre of Excellence in Exciton Science (CE170100026), the ARC Discovery Program (DP220103783), and the ARC 'LIEF' infrastructure scheme (LE210100151). The authors acknowledge the use of the instruments and scientific and technical assistance at the Monash Centre for Electron Microscopy (MCEM), a Node of Microscopy Australia, and the Monash X-ray Platform (MXP). We want to thank Dr Anthony Chesman from CSIRO Manufacturing for assistance with the ICP-MS measurement.

References

1 Pushpendra, I. Suryawanshi, S. Srinidhi, S. Singh, R. Kalia, R. K. Kunchala, S. L. Mudavath and B. S. Naidu, *Mater. Today Commun.*, 2021, **26**, 102144.
2 S. Yakunin, J. Chaaban, B. M. Benin, I. Cherniukh, C. Bernasconi, A. Landuyt, Y. Shynkarenko, S. Bolat, C. Hofer, Y. E. Romanyuk, S. Cattaneo, S. I. Pokutnyi, R. D. Schaller, M. I. Bodnarchuk, D. Poulikakos and M. V. Kovalenko, *Nat. Commun.*, 2021, **12**, 8–15.
3 A. Abdollahi, H. Roghani-Mamaqani, B. Razavi and M. Salami-Kalajahi, *ACS Nano*, 2020, **14**, 14417–14492.
4 C. B. Murray, D. J. Norris and M. G. Bawendi, *J. Am. Chem. Soc.*, 1993, **115**, 8706–8715.
5 M. Sharma, S. Delikanli and H. V. Demir, *Proc. IEEE*, 2020, **108**, 655–675.
6 Y. Wang, X. Li, J. Song, L. Xiao, H. Zeng and H. Sun, *Adv. Mater.*, 2015, **27**, 7101–7108.
7 L. Protesescu, S. Yakunin, M. I. Bodnarchuk, F. Krieg, R. Caputo, C. H. Hendon, R. X. Yang, A. Walsh and M. V. Kovalenko, *Nano Lett.*, 2015, **15**, 3692–3696.
8 T. J. Milstein, D. M. Kroupa and D. R. Gamelin, *Nano Lett.*, 2018, **18**, 3792–3799.
9 W. Liu, Q. Lin, H. Li, K. Wu, I. Robel, J. M. Pietryga and V. I. Klimov, *J. Am. Chem. Soc.*, 2016, **138**, 14954–14961.
10 K. Xu and A. Meijerink, *Chem. Mater.*, 2018, **30**, 5346–5352.
11 W. J. Mir, T. Sheikh, H. Arfin, Z. Xia and A. Nag, *NPG Asia Mater.*, 2020, **12**, 9.
12 M. İzmir, E. G. Durmusoglu, M. Sharma, F. Shabani, F. Isik, S. Delikanli, V. K. Sharma and H. V. Demir, *J. Phys. Chem. C*, 2023, **127**, 4210–4217.
13 R. Martín-Rodríguez, R. Geitenbeek and A. Meijerink, *J. Am. Chem. Soc.*, 2013, **135**, 13668–13671.
14 L. Xu, J. Chen, J. Song, J. Li, J. Xue, Y. Dong, B. Cai, Q. Shan, B. Han and H. Zeng, *ACS Appl. Mater. Interfaces*, 2017, **9**, 26556–26564.
15 D. Zhang, W. Zhou, Q. Liu and Z. Xia, *ACS Appl. Mater. Interfaces*, 2018, **10**, 27875–27884.
16 X. Feng, Y. Sheng, K. Ma, F. Xing, C. Liu, X. Yang, H. Qian, S. Zhang, Y. Di, Y. Liu and Z. Gan, *Adv. Opt. Mater.*, 2022, **10**, 1–8.
17 C. Gong, L. Lin, Y. Wu, Y. Zhang, Z. Feng, Z. Wang, Y. Huang and Z. Zheng, *J. Alloys Compd.*, 2024, **1008**, 176630.
18 X. Wang, K. Feng, L. Shan, J. Zou and B. Lu, *Opt. Express*, 2024, **32**, 14018.
19 V. T. Tuyen, B. Q. V. Huy, N. B. Tong, T. T. Ngoc Lam, M. Ferrari, C. T. My Dung, U. T. Dieu Thuy and T. T. T. Van, *RSC Adv.*, 2023, **13**, 19317–19324.
20 Z. Zeng, B. Huang, X. Wang, L. Lu, Q. Lu, M. Sun, T. Wu, T. Ma, J. Xu, Y. Xu, S. Wang, Y. Du and C. Yan, *Adv. Mater.*, 2020, **32**, 2004506.
21 G. Pan, X. Bai, D. Yang, X. Chen, P. Jing, S. Qu, L. Zhang, D. Zhou, J. Zhu, W. Xu, B. Dong and H. Song, *Nano Lett.*, 2017, **17**, 8005–8011.
22 T. Cai, J. Wang, W. Li, K. Hills-Kimball, H. Yang, Y. Nagaoka, Y. Yuan, R. Zia and O. Chen, *Adv. Sci.*, 2020, **7**, 1–9.
23 H. Arfin, J. Kaur, T. Sheikh, S. Chakraborty and A. Nag, *Angew. Chem., Int. Ed.*, 2020, **59**, 11307–11311.
24 S. Saikia, A. Ghosh and A. Nag, *Angew. Chem., Int. Ed.*, 2023, **62**, e202307689.
25 X. Cao, Y. Zhai, D. Guan, X. Wang, Q. Zhu, S. Fang, H. Zhang and L. Wang, *J. Lumin.*, 2024, **274**, 120672.
26 K. T. Kluherz, S. T. Mergelsberg, D. E. Sommer, J. Y. D. Roh, S. A. Saslow, D. Biner, K. W. Krämer, S. T. Dunham, J. J. De Yoreo and D. R. Gamelin, *Phys. Rev. Mater.*, 2022, **6**(2), 025404.
27 W. Niu, R. Zhang, Z. Wang, F. Huang and D. Chen, *Adv. Phys. Res.*, 2023, **2**, 1–9.
28 L. Fei, X. Yuan, J. Hua, M. Ikezawa, R. Zeng, H. Li, Y. Masumoto and J. Zhao, *Nanoscale*, 2018, **10**, 19435–19442.
29 M. C. De Siena, D. E. Sommer, S. E. Creutz, S. T. Dunham and D. R. Gamelin, *Chem. Mater.*, 2019, **31**, 7711–7722.
30 Y. Jing, A. K. Y. Low, Y. Liu, M. Feng, J. W. M. Lim, S. M. Loh, Q. Rehman, S. A. Blundel, N. Mathews, K. Hippalgaonkar, T. C. Sum, A. Bruno and S. G. Mhaisalkar, *Adv. Mater.*, 2024, **2405973**, 1–12.
31 N. V. Tepliakov, A. V. Sokolova, D. A. Tatarinov, X. Zhang, W. Zheng, A. P. Litvin and A. L. Rogach, *Nano Lett.*, 2024, **24**, 3347–3354.
32 D. Rossi, D. Parobek, Y. Dong and D. H. Son, *J. Phys. Chem. C*, 2017, **121**, 17143–17149.
33 X. Yuan, S. Ji, M. C. De Siena, L. Fei, Z. Zhao, Y. Wang, H. Li, J. Zhao and D. R. Gamelin, *Chem. Mater.*, 2017, **29**, 8003–8011.
34 Y. Liu, F. Di Stasio, C. Bi, J. Zhang, Z. Xia, Z. Shi and L. Manna, *Adv. Mater.*, 2024, **2312482**, 1–27.
35 Y. Zhang, D. Tu, L. Wang, C. Li, Y. Liu and X. Chen, *Mater. Chem. Front.*, 2023, **8**, 192–209.
36 S. Bera and N. Pradhan, *ACS Energy Lett.*, 2020, **5**, 2858–2872.
37 K. Xu, D. Chen, D. Huang and H. Zhu, *J. Lumin.*, 2021, **240**, 118464.
38 Y. Xing, X. Yuan, S. Ji, M. Ikezawa, R. Zeng, H. Li, Y. Masumoto and J. Zhao, *J. Lumin.*, 2018, **204**, 10–15.

39 G. Nedelcu, L. Protesescu, S. Yakunin, M. I. Bodnarchuk, M. J. Grotevent and M. V. Kovalenko, *Nano Lett.*, 2015, **15**, 5635–5640.
40 Q. A. Akkerman, V. D'Innocenzo, S. Accornero, A. Scarpellini, A. Petrozza, M. Prato and L. Manna, *J. Am. Chem. Soc.*, 2015, **137**, 10276–10281.
41 T. J. Milstein, K. T. Kluherz, D. M. Kroupa, C. S. Erickson, J. J. De Yoreo and D. R. Gamelin, *Nano Lett.*, 2019, **19**, 1931–1937.
42 K. R. Pradeep and R. Viswanatha, *APL Mater.*, 2020, **8**, 020901.
43 G. Nedelcu, L. Protesescu, S. Yakunin, M. I. Bodnarchuk, M. J. Grotevent and M. V. Kovalenko, *Nano Lett.*, 2015, **15**, 5635–5640.
44 M. D. Dogan, R. Garcia-Martin, P. W. Haertel, J. J. O'Keefe, A. Taka, A. Aurora, R. Sanchez-Reillo and S. Mueller, *BrightMarker: 3D Printed Fluorescent Markers for Object Tracking*, Association for Computing Machinery, 2023, vol. 1.